Linked-cluster expansion for the Green's function of the infinite-U Hubbard model

Ehsan Khatami,[1,2] Edward Perepelitsky,[1] Marcos Rigol,[3] and B. Sriram Shastry[1]
[1]*Department of Physics, University of California, Santa Cruz, California 95064, USA*
[2]*Department of Physics, University of California, Davis, California 95616, USA*
[3]*Department of Physics, The Pennsylvania State University, University Park, Pennsylvania 16802, USA*
(Received 3 December 2013; revised manuscript received 16 April 2014; published 2 June 2014)

We implement a highly efficient strong-coupling expansion for the Green's function of the Hubbard model. In the limit of extreme correlations, where the onsite interaction is infinite, the evaluation of diagrams simplifies dramatically enabling us to carry out the expansion to the eighth order in powers of the hopping amplitude. We compute the finite-temperature Green's function analytically in the momentum and Matsubara frequency space as a function of the electron density. Employing Padé approximations, we study the equation of state, Kelvin thermopower, momentum distribution function, quasiparticle fraction, and quasiparticle lifetime of the system at temperatures lower than, or of the order of, the hopping amplitude. We also discuss several different approaches for obtaining the spectral functions through analytic continuation of the imaginary frequency Green's function, and show results for the system near half filling. We benchmark our results for the equation of state against those obtained from a numerical linked-cluster expansion carried out to the eleventh order.

DOI: 10.1103/PhysRevE.89.063301 PACS number(s): 02.60.−x, 71.10.Fd, 71.27.+a

I. INTRODUCTION

In 1991, Metzner put forth an algorithm to compute the finite-temperature Green's function of the Fermi-Hubbard model [Eq. (1)] through a linked-cluster strong-coupling expansion [1]. His approach offers a relatively straightforward implementation on a computer, which is particularly useful today given the enormous improvements in computer power in the past two decades. The Metzner formalism further simplifies in the limit of extreme correlations, as the onsite repulsion U tends to infinity. In this paper, we implement his approach to obtain analytical expressions for the single-particle Green's function in that limit through eighth order in the expansion parameter βt, where β is the inverse temperature and t is the hopping amplitude of the electrons on the lattice.

In another recent development, the extremely correlated Fermi liquid theory (ECFL) [2] addresses this important limit through the use of Schwinger's source formulation of field theory. One of the significant physical ideas to come out of this theory is the presence of particle-hole asymmetry in the spectral densities of the single-particle Green's function and the Dyson-Mori self-energy [2–8]. This asymmetry, which has also been observed in dynamical mean-field theory studies of the Hubbard model [7,9,10], becomes more pronounced as the density approaches half-filling, i.e., as $n \to 1$. The asymmetry has implications for understanding the magnitude and sign of the Seebeck coefficient near the Mott insulating limit [10–12] and for explaining the anomalous line shapes of angle-resolved photoemission spectroscopy experiments [13] in strongly correlated materials.

In a recent work [14], the present authors (with Hansen) used the series expansion method to successfully benchmark the ECFL results for the spectral function [5], in their common regime of applicability. The currently available $[O(\lambda^2)]$ self-consistent solution of the ECFL is valid for $n \lesssim 0.75$. Additionally, the insight afforded by the aforementioned particle-hole asymmetry enabled us to construct a suitably modified first moment of the spectral function, providing a good estimate for the location of the quasiparticle peak. This moment reduces the contribution from the occupied side of the spectrum relative to the unoccupied side, leading to a sharper location of the peaks. Therefore, using the series expansion to calculate this moment, we were able to study the dispersion of the quasiparticle energy and, as a result, the evolution of the Fermi surface in the limit $n \to 1$, i.e., beyond the density regime currently accessible to the $O(\lambda^2)$ version of the ECFL.

Here, we expand upon our previous findings and perform analytic continuation to obtain the full spectral functions. Direct analytic continuation of finite series, however, leads to unphysical results, e.g., negative spectral functions can arise due to the truncation of the series. This is a well-studied problem with known resolutions [15,16]. Therefore, and in particular, to ensure the positivity of spectral densities, we either take advantage of a transformation that guarantees this positivity, or assume an approximate form for the spectral functions, which comes out of the ECFL. We find a good agreement between results from the two approaches, which capture the expected features of the spectra discussed above.

Using strong-coupling expansions, there have been several earlier studies of the thermodynamics and time-independent correlations of the Hubbard and related models [17]. However, strong-coupling expansions for the *time-dependent correlations* are very rare [16,18,19]. In Ref. [16], the authors carried out a strong-coupling expansion for the Green's function to fifth order in βt for the finite-U Hubbard model. Here, the simplifications arising from the $U \to \infty$ limit allow us to go to eighth order in βt. This provides us with the opportunity to employ Padé approximations and study several static and dynamic quantities, such as the equation of state, momentum distribution function, the quasiparticle fraction, and lifetime at temperatures lower than the hopping amplitude, where the direct sums in the series do not converge. We also take advantage of the state-of-the-art numerical linked-cluster expansions (NLCEs) [20], developed recently for the t-J model, and set the exchange interaction J to 0, to gauge our low-temperature equation of state obtained from the Padé approximations.

The organization of the paper is as follows: In Secs. II and III, we review the Metzner formalism and detail its numerical implementation. In Sec. IV, we provide analytical expressions for the Green's function and the Dyson-Mori self-energy in momentum and Matsubara frequency space as a function of the density. In Sec. V, we discuss the convergence of the series both before and after the use of Padé approximations. Additionally, using the series, we report results for the time-dependent local Green's function, the equation of state, Kelvin thermopower, the quasiparticle weight at the Fermi surface, momentum occupation number, and quasiparticle lifetime and spectral functions at different points along the irreducible wedge of the Brillouin zone. We summarize our results in Sec. VII.

II. THE MODEL

In the strong-coupling limit, the Hubbard Hamiltonian is written as the sum of the unperturbed local Hamiltonian H_0, and a perturbation H_1 that accounts for hopping of electrons between the sites of the lattice,

$$H = H_0 + H_1, \tag{1}$$

where

$$\begin{aligned} H_0 &= U \sum_i n_{i\uparrow} n_{i\downarrow} - \mu \sum_{i\sigma} n_{i\sigma}, \\ H_1 &= -\sum_{ij\sigma} t_{ij} c^\dagger_{i\sigma} c_{j\sigma}. \end{aligned} \tag{2}$$

Here, $c_{i\sigma}$ ($c^\dagger_{i\sigma}$) annihilates (creates) a fermion with spin σ on site i, $n_{i\sigma} = c^\dagger_{i\sigma} c_{i\sigma}$ is the number operator, U is the onsite repulsive Coulomb interaction, μ is the chemical potential, and t_{ij} is the hopping matrix element between sites i and j. As discussed in the following, we allow for nearest-neighbor hopping only, namely, $t_{ij} = t$ if i and j are nearest neighbors, and $t_{ij} = 0$ otherwise.

III. METZNER'S APPROACH FOR COMPUTING THE GREEN'S FUNCTION

We start by describing the Metzner formalism before turning our focus to topics related to its computational implementation in the limit of extreme correlations. Following the conventions in Ref. [1], we define the finite-temperature single-particle Green's function as

$$G_{\sigma jj'}(\tau - \tau') = -\langle T_\tau c_{j\sigma}(\tau) c^\dagger_{j'\sigma}(\tau') \rangle, \tag{3}$$

where $\langle .. \rangle$ denotes the thermal average with respect to H, T_τ denotes the imaginary time-ordering operator, and the creation and annihilation operators in the Heisenberg representation are expressed as

$$\begin{aligned} c^\dagger_{j\sigma}(\tau) &= e^{H\tau} c^\dagger_{j\sigma} e^{-H\tau}, \\ c_{j\sigma}(\tau) &= e^{H\tau} c_{j\sigma} e^{-H\tau}, \end{aligned} \tag{4}$$

where $0 \leqslant \tau \leqslant \beta$ is an imaginary time variable.

To derive a perturbative expansion for $G_{\sigma jj'}(\tau - \tau')$, we switch to the interaction representation, where the time evolution of the operators is governed by the unperturbed Hamiltonian H_0. The Green's function can then be expressed as

$$G_{\sigma jj'}(\tau - \tau') = -\langle T_\tau c_{j\sigma}(\tau) c^\dagger_{j'\sigma}(\tau') \mathcal{S} \rangle_0 / \langle \mathcal{S} \rangle_0, \tag{5}$$

where the expectation values ($\langle .. \rangle_0$) are taken with respect to the unperturbed Hamiltonian, and $\mathcal{S}$ is given by

$$\mathcal{S} = T_\tau \exp\left[\int_0^\beta d\tau \sum_{ij\sigma} t_{ij} c^\dagger_{i\sigma}(\tau) c_{j\sigma}(\tau) \right]. \tag{6}$$

Next, by expanding the exponential in Eq. (6), both the numerator and the denominator of Eq. (5) can be written as perturbative series expansions in t. As detailed in Ref. [1], every term of the expansions can be written in terms of cumulants (connected many-particle Green's functions) of the unperturbed system, denoted by C^0_m (m indicates the number of creation or destruction operators in the cumulant). Due to the local nature of the unperturbed Hamiltonian, the cumulants are site diagonal, i.e., the only nonzero ones are those whose site variables are the same, and they can therefore be indexed by site. Due to the translational invariance of the Hamiltonian, an order m cumulant at site i is independent of i and is a function of only the time and spin indices of the m creation, and m destruction operators acting on i, i.e., $C^0_{mi} \equiv C^0_m(\tau_1\sigma_1, \ldots \tau_m\sigma_m | \tau'_1\sigma'_1, \ldots \tau'_m\sigma'_m)$. As we will see in the following, this invariance is a major advantage of the present method. Using it, each term in the expansion can be written as a product of a spatial part and a temporal part, which may then be evaluated independently.

The terms in the expansion for $\langle \mathcal{S} \rangle_0$ can be evaluated using a diagrammatic approach, where each diagram consists of vertices, and directed lines connecting the vertices. Each vertex represents a site on the lattice, and each line represents a hopping process between two sites. Furthermore, the spatial sums reduce to calculating free multiplicities of graphs when embedded on the lattice. This computationally inexpensive part of the algorithm can be carried out independently of the most expensive part (taking the time integrals), for *any* lattice geometry.

The expectation value in the numerator of Eq. (5) can be calculated the same way as $\langle \mathcal{S} \rangle_0$, except that any graph in the former contains two additional *external* lines, one entering the site j' at time τ' and one exiting the site j at time τ. Consequently, in the lattice sums, one has to "fix" the vertices to which the external lines attach to be the sites j and j' on the lattice with the desired separation between them.

Another important feature of this method is the fact that the spatial sums are unrestricted (different vertices are allowed to be on the same lattice site), and therefore it can be verified that the contributions of disconnected diagrams are products of the contributions of their connected components (the linked-cluster theorem holds). Hence, the disconnected diagrams in the numerator of Eq. (5) are canceled by the denominator, and $G_{\sigma jj'}(\tau, \tau')$ is given as the sum of the contributions of only the connected graphs in its numerator.

Further details of the method are given in Ref. [1] and will not be repeated here. The rules mentioned in Ref. [1] for generating the graphs and evaluating their contributions are reproduced below.

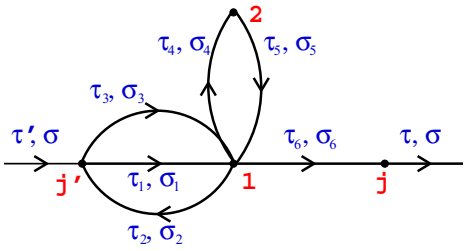

FIG. 1. (Color online) Diagram of a sample graph in the sixth order (with six internal and two external lines). The time and spin indices of lines are ordered according to rule (iii). To calculate the contribution of this graph, we need to insert C_2^0, C_3^0, C_1^0, and C_1^0 for vertices j', 1, 2, and j, respectively, for the time integral and the spin sum, and $(t_{j'1})^3(t_{12})^2 t_{1j}$ for the spatial sum. The symmetry factor is 2 since exchanging lines that correspond to $\tau_1\sigma_1$ and $\tau_3\sigma_3$ does not change the topology of the graph.

A. Rules for calculating the one-particle Green's function diagrammatically

(i) Draw all topologically distinct diagrams: vertices connected by directed lines such that the number of entering and exiting lines at each vertex is the same. The graphs consist of the internal lines that connect two vertices as well as two *external* lines that enter a vertex and exit a vertex. The order to which each graph contributes is equal to the number of internal lines it has.

(ii) Label each line with a time and spin index, and each vertex by a lattice index. The vertex that has the entering external line is labeled by j' and the vertex that has the exiting external line is labeled by j.

(iii) Order the lines by defining a path that starts from the entering external line at vertex j', goes through all of the vertices, and ends with the exiting external line at j. Figure 1 shows an example of such a graph in the sixth order.

(iv) Insert a factor of $(-t_{il})$ for each line that connects vertex i to vertex l.

(v) Insert $C_m^0(\tau_1\sigma_1,\ldots\tau_m\sigma_m|\tau_1'\sigma_1',\ldots\tau_m'\sigma_m')$ for each vertex that has m entering lines labeled $\tau_1'\sigma_1',\ldots\tau_m'\sigma_m'$ and m exiting lines labeled $\tau_1\sigma_1,\ldots\tau_m\sigma_m$, such that $\tau_i\sigma_i$ corresponds to the next line after $\tau_i'\sigma_i'$ according to the ordering defined in (iii). This will ensure that there are no fermion loops in the diagram.

(vi) Determine the symmetry factor of the graph, which is the number of permutations of labeled lines and vertices that do not change its topology.

(vii) To calculate the contribution of the graph, integrate each *internal* time index between 0 and β, sum over the *internal* spatial and spin indices, and divide the result by the symmetry factor. As an example, the contribution of the graph c in Fig. 1 is

$$\begin{aligned} W(c) = \frac{1}{2}\sum_{1,2}(t_{j'1})^3(t_{12})^2 t_{1j}\int_0^\beta d\tau_1\ldots\int_0^\beta d\tau_6 \\ \times\sum_{\sigma_1\ldots\sigma_6} C_2^0(\tau_1\sigma_1,\tau_3\sigma_3|\tau'\sigma,\tau_2\sigma_2) \\ \times C_3^0(\tau_2\sigma_2,\tau_4\sigma_4,\tau_6\sigma_6|\tau_1\sigma_1,\tau_3\sigma_3,\tau_5\sigma_5) \\ \times C_1^0(\tau_5\sigma_5|\tau_4\sigma_4)\,C_1^0(\tau\sigma|\tau_6\sigma_6). \end{aligned} \tag{7}$$

(viii) To obtain the lth-order contribution to the Green's function, add the contributions $W(c)$, of all the graphs with l internal lines:

$$G^{(l)} = \sum_{c\,\in\,\text{order }l} W(c). \tag{8}$$

In this scheme, the only zeroth-order graph consists of a vertex and the two external lines. In the first order, the only possible topology has two vertices, each having an external line, and a single internal line connecting them. In higher orders, the number of vertices can vary from two to $l+1$, where l denotes the order, depending on the topology. The topologically distinct graphs up to the fourth order are shown in Fig. 4 of Ref. [1].

B. Computational implementation

We have implemented a computer program to perform all of the steps described in Sec. III A for the infinite-U case. In this limit, since no double occupancy is allowed, the calculation of the cumulants simplifies drastically. This enables us to carry out the expansion to eighth order. In this subsection, we explain some of the details of this implementation at each step.

1. Generation of topologically distinct graphs

To generate all topologically distinct diagrams in step (i) above, we need to have a way of uniquely identifying them in a computer program. For this, we use the concept of adjacency matrices. The elements of a $m\times m$ adjacency matrix, where m is the number of vertices, represent the connections between every two vertices. For instance, for a graph with undirected lines between vertices, the (i,j) element can be an integer that simply counts the number of lines between vertices i and j. Here, since the lines are directed, we use a generalization of this matrix where every element is replaced by an array of size two. The first element of this array (we call it the left element) represents the number of incoming lines from vertex i to vertex j while the second element (or the right element) represents the number of outgoing lines from vertex j to vertex i.

One has to note that a topologically distinct graph cannot be uniquely represented by such an adjacency matrix since different labelings of the vertices, while not altering the topology, lead to different adjacency matrices. Therefore, one has to devise an algorithm to pick only one, out of $m!$ possibilities, of the labelings of a graph to be able to establish a one-to-one correspondence between the graphs and its adjacency matrix. This can be done, for example, through *sorting* the adjacency matrix; by assigning the first row (column) to the vertex that possesses the largest number of lines, and so on. Alternatively, in our case, we can more simply employ the order of vertices that results from rule (iii) above.

After defining the mapping between the adjacency matrices and graphs in the computer algorithm, we generate graphs with m vertices by considering all possible numbers for the elements of the $m\times 2m$ adjacency matrix, subject to the following two constraints: First, the number of incoming and outgoing lines at each vertex have to be the same, so, if we subtract the sum of left elements and the sum of right elements at each row (column) the result has to be zero. Second, the total

number of lines in the graph (or the sum of all elements of the matrix, divided by 2) should be equal to the desired order in the expansion. Note that, in this strong-coupling expansion, there is no line that leaves a vertex and then enters the same vertex, i.e., the diagonal elements of all adjacency matrices are zero.

2. Cumulants

We obtain cumulants to any order by taking functional derivatives of the generating functional with respect to Grassmann variables as described in Refs. [1,21]. As a result, a cumulant of order l is written in terms of the local unperturbed Green's function (UGF) of the same order G_l^0, as well as lower order UGFs. In Appendix A, we show this expansion for the first few cumulants. The calculation of the cumulants then reduces to the evaluation of the UGFs, which, for order l, is the expectation value of $2l$ time-ordered creation and annihilation operators with respect to the unperturbed Hamiltonian. For our case of the infinite-U limit, since no double occupancy is allowed, a creation operator can only be followed by an annihilation operator and vice versa. Hence, the Green's function can assume only two distinct values depending on whether a creation or an annihilation operator is on the right side of the time-ordered product of operators. The two values are, respectively, $(1-\rho)$ and $\frac{\rho}{2}$, where $\rho = \frac{2e^{\beta\mu}}{1+2e^{\beta\mu}}$ is the density in the atomic limit. For example, we end up with the following terms for the first two orders:

$$G_1^0(\tau_1\sigma_1|\tau_1'\sigma_1') = \langle T_\tau c^\dagger_{j\sigma_1'}(\tau_1')c_{j\sigma_1}(\tau_1)\rangle = e^{\mu(\tau_1-\tau_1')}\delta_{\sigma_1\sigma_1'}\left[\frac{\rho}{2}\Theta(\tau_1'-\tau_1)-(1-\rho)\Theta(\tau_1-\tau_1')\right], \tag{9}$$

$$\begin{aligned} G_2^0(\tau_1\sigma_1,\tau_2\sigma_2|\tau_1'\sigma_1',\tau_2'\sigma_2') &= \langle T_\tau c^\dagger_{j\sigma_1'}(\tau_1')c_{j\sigma_1}(\tau_1)c^\dagger_{j\sigma_2'}(\tau_2')c_{j\sigma_2}(\tau_2)\rangle \\ &= e^{\mu(\tau_1+\tau_2-\tau_1'-\tau_2')}\sum_{qp}(-1)^q(-1)^p\left[\frac{\rho}{2}\delta_{q\sigma_2 p\sigma_1'}\delta_{q\sigma_1 p\sigma_2'}\Theta(p\tau_1'-q\tau_1)\Theta(q\tau_1-p\tau_2')\Theta(p\tau_2'-q\tau_2)\right. \\ &\quad \left.+(1-\rho)\delta_{q\sigma_2 p\sigma_2'}\delta_{q\sigma_1 p\sigma_1'}\Theta(q\tau_1-p\tau_1')\Theta(p\tau_1'-q\tau_2)\Theta(q\tau_2-p\tau_2')\right], \end{aligned} \tag{10}$$

where the sum runs over permutations p and q of the time and spin indices of the primed and unprimed variables, respectively, and Θ is the usual step function.

3. Free multiplicities

The spatial sums are performed for a specific lattice geometry. We have calculated them on the square lattice. In the computer program, we define a large enough lattice where we can fit any cluster with a number of sites at least twice as large as the maximum number of vertices in our largest order graphs. We then assign vertices j' (where an external line enters) and j (where an external line exits) to two lattice sites with a given displacement between them. The next part of the algorithm involves finding the number of possibilities for assigning the rest of the vertices to lattice sites. This can be done by following the path we have defined for each graph in rule (iii) to go from vertex j' to j. We start from vertex j' and in each step, we move to the next vertex in the list and assign a site to it. We ensure that if we come back to a vertex in the graph, we also come back to the corresponding site on the lattice. However, since we are calculating free multiplicities, we can assign the same lattice site to multiple vertices wherever the topology of the graph allows for it. In Table I, we show the number of topologically distinct graphs in each order, along with the number of graphs that have nonzero contributions on bipartite geometries, and the sum of free multiplicities for all graphs in each order for the (0,0) and (1,0) separations, up to the 10th order.

This computationally inexpensive process can be repeated for all possible separations (the maximum separation is set by the largest order considered). They can then be used to calculate the Fourier transform of the Green's function into the momentum space.

4. Time integrals

As seen in Sec. III B 2, the cumulants for the infinite-U Hubbard model consist of products of only step functions and exponentials in the internal and external imaginary times. After multiplying several cumulants to obtain the contribution of a graph, we typically end up with a huge number of terms, each consisting of the product of a set of step functions of the time variables, the exponentials associated with the external times (the exponentials associated with the internal times cancel), Kronecker delta functions of the spin indices, and a function

TABLE I. Total number of topologically distinct graphs (second column), number of graphs that have nonzero multiplicity on bipartite geometries (third column), and the sum of multiplicities of all graphs for the smallest separations for which they have nonzero multiplicity (fourth column) at each order. The smallest separation for graphs with even number of lines (in even orders) is $r_{j'}-r_j=(0,0)$, and for graphs in odd orders is considered to be $r_{j'}-r_j=(1,0)$.

Order	Topologically distinct	Used for bipartite	$\sum$ Multiplicities
0	1	1	1
1	1	1	1
2	2	2	8
3	5	4	18
4	14	10	164
5	41	22	458
6	130	59	4240
7	431	146	13 544
8	1512	425	130 516
9	5542	1136	448 211
10	21 236	3497	4 408 216

of ρ. As mentioned before, one of the main advantages of our approach is that the time integrals over internal time variables can be taken independently of the spatial sums (free multiplicity calculations). We choose $\tau' = 0$ without loss of generality since the Green's function is a function of $\tau - \tau'$ and $G(\tau - \tau' < 0)$ can be obtained from $G(\tau - \tau' > 0)$ using the antiperiodicity of the Green's function in imaginary time [22]. To see how the time integrals are evaluated, we proceed with the following example. Suppose that one of the terms that belongs to a graph in the third order can be written as

$$\mathcal{I}(\tau) = \int_0^\beta \int_0^\beta \int_0^\beta d\tau_1 d\tau_2 d\tau_3 \Theta(\tau_1 - \tau_3)\Theta(\tau - \tau_3). \quad (11)$$

Note that in the above example, we have a smaller number of step functions in the integrand than typically expected for a term in the third order. However, the above combination is a perfectly valid one as the products of step functions are often simplified given that $\Theta^n(x) = \Theta(x)$ for any nonzero n. The integral over τ_2 yields a factor β as there is no restriction on τ_2. The remaining integrals are nonzero if $\tau_1 > \tau_3$ and $\tau > \tau_3$. But, the latter condition does not uniquely determine the position of τ_1 relative to τ in the $[0,\beta]$ interval. Therefore, we consider the two possibilities, $\tau > \tau_1$ and $\tau < \tau_1$, and rewrite the integral of Eq. (11) as

$$\mathcal{I}(\tau) = \beta \int_0^\beta \int_0^\beta d\tau_1 d\tau_3 \times [\Theta(\tau_1 - \tau)\Theta(\tau - \tau_3) + \Theta(\tau - \tau_1)\Theta(\tau_1 - \tau_3)]. \quad (12)$$

Note that for any value of τ_1 and τ_3, only one of the terms in the integral in Eq. (12) is nonzero, justifying the equality. At this point, we can use the known results for the types of integrals in Eq. (12) (see Appendix B), leading to $\beta[\tau(\beta - \tau) + \frac{\tau^2}{2!}]$.

Computationally, the two distinct possibilities for the ordering of times in the above example can be found by generating all of the permutations of the time indices, and for each permutation, examining whether every step function in the product is nonzero. If that is the case, a multiplication of step functions corresponding to that permutation is inserted as the integrand.

5. *Symmetry factor*

Calculating the symmetry factor of each graph is straightforward in the framework of adjacency matrices. First, we note that the symmetry factor is proportional to the factorials of elements of the adjacency matrix in its upper triangle as they correspond to the number of permutations of directed lines that do not change the topology of the graph. Second, in order to find the symmetry factor related to those permutations of labeled vertices that leave the graph topology intact, we simply generate all the $m!$ matrices that correspond to different orderings of vertex labels and find how many of them are the same as the original matrix. We then multiply this number by the factorials calculated in the first step to obtain the symmetry factor of the graph.

IV. ANALYTICAL RESULTS

After evaluating the contribution of each diagram in a particular order by multiplying its free multiplicity for a given separation, time integral, and the spin sum, and dividing it by the symmetry factor, we add all of those contributions for that order to form the Green's function in terms of the atomic density ρ, the imaginary time τ, t, μ, and β. By calculating the spatial sums for all possible separations for each graph and performing a Fourier transformation on the space and imaginary time, one can express the Green's function in terms of the momentum k, and the Matsubara frequency ω_n. Below, we show the resulting Green's function in the first four orders [23]:

$$\begin{aligned}
G_\sigma^{(0)}(z,k) &= \frac{1-\frac{\rho}{2}}{z},\\
G_\sigma^{(1)}(z,k) &= \frac{\left(1-\frac{\rho}{2}\right)^2\epsilon_k}{z^2},\\
G_\sigma^{(2)}(z,k) &= \frac{\left(1-\frac{\rho}{2}\right)^3\epsilon_k^2}{z^3} + \frac{(4-\rho)\rho\left(1-\frac{\rho}{2}\right)t^2}{z^3} - \frac{2\beta(\rho-1)\rho t^2}{z^2} + \frac{\beta^2\rho[(3-2\rho)\rho-1]t^2}{z},\\
G_\sigma^{(3)}(z,k) &= \frac{\left(1-\frac{\rho}{2}\right)^4\epsilon_k^3}{z^4} - \frac{7(\rho-4)\rho(\rho-2)^2t^2\epsilon_k}{16z^4} + \frac{3\beta(\rho-1)\rho(\rho-2)t^2\epsilon_k}{2z^3} + \frac{\beta^2(\rho-1)\rho[\rho(7\rho-19)+8]t^2\epsilon_k}{4z^2},\\
G_\sigma^{(4)}(z,k) &= \frac{\left(1-\frac{\rho}{2}\right)^5\epsilon_k^4}{z^5} + \frac{5(\rho-4)\rho(\rho-2)^3t^2\epsilon_k^2}{16z^5} - \frac{\rho\{\rho[(\rho-8)\rho-152]+240\}(\rho-2)t^4}{8z^5}\\
&\quad - \frac{\beta(\rho-1)\rho(\rho-2)^2t^2\epsilon_k^2}{z^4} + \frac{\beta(\rho-1)\rho[\rho(4\rho+11)-16]t^4}{z^4} - \frac{\beta^2(\rho-1)\rho[\rho(5\rho-14)+6](\rho-2)t^2\epsilon_k^2}{4z^3}\\
&\quad + \frac{\beta^2(\rho-1)\rho\{\rho[2\rho(5\rho-24)+43]-16\}t^4}{2z^3} - \frac{\beta^3(\rho-1)\rho[\rho(97\rho-100)+18]t^4}{6z^2}\\
&\quad - \frac{\beta^4(\rho-1)\rho\{\rho[\rho(388\rho-591)+236]-18\}t^4}{24z}\\
&\vdots\ ,
\end{aligned} \quad (13)$$

where $z = i\omega_n + \mu$, and $\epsilon_k = -2t[\cos(k_x) + \cos(k_y)]$. Note that in this format, the Green's function is written in terms of the atomic density ρ or equivalently the chemical potential μ, and not the true density for the many-body system, $n = 1 + G_{jj\sigma}(\tau - \tau' = 0^+, \mu)$ [25]. By definition, n, too, can be written as an expansion in the hopping (using the expansion for the local Green's function). However, we would like to treat n as a parameter and rewrite the Green's function in terms of it. In that case, the chemical potential can no longer remain constant and we have to solve for it order by order in terms of n and t: $\mu = \mu^{(0)} + \mu^{(2)} + \mu^{(4)} \ldots$ where

$$n - 1 = G^{(0)}_{jj\sigma}(0^+,\mu^{(0)}) + G^{(2)}_{jj\sigma}(0^+,\mu^{(0)}) + \left.\frac{dG^{(0)}_{jj\sigma}(0^+,\mu)}{d\mu}\right|_{\mu=\mu^{(0)}} \mu^{(2)} + G^{(4)}_{jj\sigma}(0^+,\mu^{(0)}) + \left.\frac{dG^{(2)}_{jj\sigma}(0^+,\mu)}{d\mu}\right|_{\mu=\mu^{(0)}} \mu^{(2)}$$
$$+ \frac{1}{2}\left.\frac{d^2G^{(0)}_{jj\sigma}(0^+,\mu)}{d\mu^2}\right|_{\mu=\mu^{(0)}} (\mu^{(2)})^2 + \left.\frac{dG^{(0)}_{jj\sigma}(0^+,\mu)}{d\mu}\right|_{\mu=\mu^{(0)}} \mu^{(4)} + \cdots \tag{14}$$

Inverting this equation for μ in terms of n, we obtain

$$\mu^{(0)} = \frac{1}{\beta}\log\frac{n}{2(1-n)}, \quad \mu^{(2)} = 2(2n-1)t^2\beta, \quad \mu^{(4)} = \frac{1}{12}(6 + n(n-4)(1+4n))t^4\beta^3$$
$$\vdots \tag{15}$$

Finally, by inserting these back into the expansion for the momentum- and frequency-dependent Green's function order by order, we end up with the following terms for up to the fourth order [26]:

$$G^{(0)}_\sigma(z,k) = \frac{1-\frac{n}{2}}{z},$$
$$G^{(1)}_\sigma(z,k) = \frac{\left(1-\frac{n}{2}\right)^2\epsilon_k}{z^2},$$
$$G^{(2)}_\sigma(z,k) = \frac{\left(1-\frac{n}{2}\right)^3\epsilon_k^2}{z^3} + \frac{[2(n-2)-n][2(n-1)-n]nt^2}{2z^3} - \frac{[2(n-1)+n]t^2\beta}{z^2},$$
$$G^{(3)}_\sigma(z,k) = \frac{\left(1-\frac{n}{2}\right)^4\epsilon_k^3}{z^4} - \frac{7[2(n-2)-n]n(2-n)^2t^2\epsilon_k}{16z^4} - \frac{[2(n-1)-n][2(2-3n)+(n-1)n]t^2\beta\epsilon_k}{2z^3} - \frac{(n-1)^2n^2t^2\beta^2\epsilon_k}{4z^2},$$
$$G^{(4)}_\sigma(z,k) = +\frac{\left(1-\frac{n}{2}\right)^5\epsilon_k^4}{z^5} + \frac{5[2(n-2)-n][2(n-1)-n]^3nt^2\epsilon_k^2}{16z^5} + \frac{[2(n-1)-n]n(-n^3+8n^2+152n-240)t^4}{8z^5}$$
$$+ \frac{\{4(n-1)n - 6[2(n-1)+n]\}(2-n)^2t^2\beta\epsilon_k^2}{8z^4}$$
$$+ \frac{n\{2[-3n^2+6(2n-3)n+4(n-1)(9n-10)]+(1-n)n(4n+2)\}t^4\beta}{2z^4}$$
$$+ \frac{[4(2n^3+6n^2-10n+4)-(n-1)n^2(4n^2-12n+2)]t^4\beta^2}{4z^3} + \frac{(-6n^3+68n^2-20n-24)t^4\beta^3}{48z^2}$$
$$\vdots\ , \tag{16}$$

where $z = i\omega_n + \mu^{(0)}$. It is perhaps even more useful to extract a self-energy from this expansion. The Dyson-Mori self-energy (denoted simply with $\Sigma_{\rm DM} \to \Sigma$) can be deduced using $\Sigma(z,k) = z - a_G[\epsilon_k + G(z,k)^{-1}]$, where $a_G = (1 - n/2)$ [3].

$$\Sigma^{(0)}(z,k) = 0$$
$$\Sigma^{(1)}(z,k) = 0$$
$$\Sigma^{(2)}(z,k) = \frac{t^2\beta(6n-4)}{n-2} - \frac{(n^2-4n)t^2}{z}$$
$$\Sigma^{(3)}(z,k) = \frac{n^2t^2\epsilon_k\beta^2(1+n^2-2n)}{2(n-2)} - \frac{(n-4)(n-2)nt^2\epsilon_k}{8z^2} + \frac{nt^2\epsilon_k\beta(n-1)}{z}$$
$$\Sigma^{(4)}(z,k) = \frac{t^4\beta^3(12+3n^3-34n^2+10n)}{12(n-2)} - \frac{3(n^4-8n^3+72n^2-80n)t^4}{4z^3}$$
$$+ \frac{2t^4\beta(2n^4-40n^3+65n^2-24n)}{(n-2)z^2} + \frac{t^4\beta^2(2n^6-12n^5+19n^4-19n^3+10n^2)}{(n-2)^2z}$$
$$\vdots \tag{17}$$

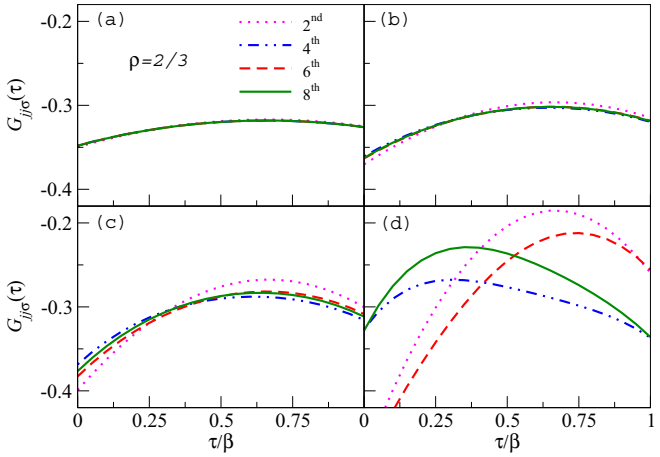

FIG. 2. (Color online) Local Green's function for a constant chemical potential $\mu = 0$ vs imaginary time at (a) $T = 3.0$, (b) $T = 2.0$, (c) $T = 1.5$, and (d) $T = 1.0$. $t = 1$ is the unit of energy throughout the paper.

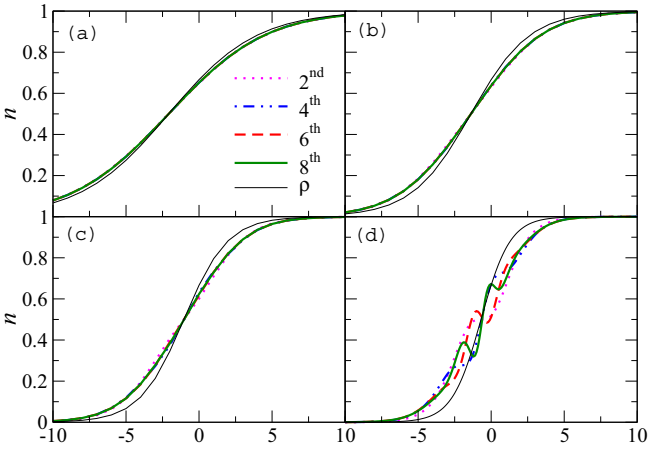

FIG. 3. (Color online) Density n as a function of the chemical potential at (a) $T = 3.0$, (b) $T = 2.0$, (c) $T = 1.5$, and (d) $T = 1.0$. Thin solid lines are the density in the atomic limit, $\rho = \frac{2e^{\beta\mu}}{1+2e^{\beta\mu}}$.

V. CONVERGENCE AND THE PADÉ APPROXIMATION

In Fig. 2, we show the local imaginary time Green's function for $\rho = 2/3$, corresponding to $\mu = 0$, at different temperatures. At $T = 3.0$ (unless specified otherwise, we take $t = 1$ as the unit of energy and work in units where $k_B = 1$ throughout the paper), the series show very good convergence as expected in this high-temperature region. Note that odd terms in the series are zero for this local quantity. As we lower T to 2.0, there are some discrepancies between low orders, but the last two orders (6 and 8) still agree very well. This is no longer the case as we get closer to $T = 1$, below which the finite series is divergent by definition. This is because in the absence of any other energy scale in the system, an expansion in t can be viewed as an expansion in β. In other words, β^{m+1} always couples to t^m in the series for the Green's function. In Fig. 2(d), one can see large fluctuations between different orders already at $T = 1.0$ and there is no clear picture from the bare results as to what the actual shape of the Green's function is.

To demonstrate the trends in the convergence of the series at other values of μ, in Fig. 3, we show the equation of state at the same four temperatures as in Fig. 2. We also show the equation of state in the atomic limit (ρ vs μ). We find that the last two orders more or less agree with each other for all μ at $T \gtrsim 1.5$. However, for $T = 1$, the convergence is lost in the vicinity of $\mu = 0$. This shows that the poor convergence of the local Green's function at this value of μ, seen in Fig. 2(d), represents the worst case scenario. An important feature of the equation of state as observed in Fig. 3 is that even at these high temperatures, there are significant deviations of the many-body density from the density in the atomic limit near the extreme limits of $n = 0$ and $n = 1$.

It is instructive now to study the temperature dependence of the density at a given μ, and to find out how the region of convergence can be extended in temperature by the use of Padé approximations. In Fig. 4, we show the temperature dependence of the density for various positive and negative values of μ. We show the direct sums as well as results after two different Padé approximations. The results in the atomic limit [$\rho(T)$] are shown for $\mu = 0$ and ± 2.0. In the atomic limit, the system has two ground states depending on the sign of μ. They correspond to $\rho = 1$ and $\rho = 0$ for positive and negative μ, respectively. At exactly $\mu = 0$, ρ is temperature independent at $2/3$. As one can see in Fig. 4, the real density for the many-body system has a qualitatively different behavior than ρ starting at relatively high temperatures. The temperature where n starts deviating from ρ due to correlations is around $T \sim 2$ for $\mu = -2$ and $T \sim 5$ for $\mu = 2$. As expected, the density for $\mu = 0$ falls below $2/3$ for all T. To perform Padé approximation for n vs T, we first expand ρ, i.e., the

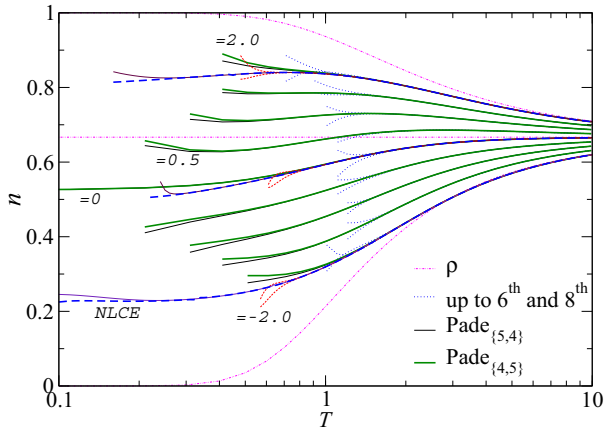

FIG. 4. (Color online) Average density n as a function of temperature for a range of μ from -2.0 to 2.0, with the increment of 0.5. The two indices of Padé in curly brackets indicate the order of the polynomials in the numerator and the denominator. From bottom to top, the dotted-dashed magenta lines are ρ for $\mu = -2$, 0, and 2. We are also showing results from the NLCE for these three values of the chemical potential as thin dashed red lines (last two orders of the bare sums), and thick dashed blue and thin solid violet lines (after Wynn resummations with five and four cycles of improvement, respectively) [20].

zeroth-order term, in powers of β and then add the rest of the higher order terms from the series. Therefore, in the case of $\mu = 0$, where ρ is temperature independent, the odd powers of β in the series for n vanish and the two Padé approximants yield the same function, leading to $n \sim 0.525$ for the ground state. Nevertheless, we cannot verify that this is the true value of the ground-state density of the system for $\mu = 0$.

The static properties of the model, such as the density, can in principle be obtained in higher orders by avoiding the relatively difficult calculation of the Green's function, and calculating only the free energy instead. However, for this purpose, we can also take advantage of the novel NLCE method that has been developed in recent years [20]. NLCE uses the same basis as high-temperature expansions, but calculates properties of finite clusters exactly, as opposed to perturbatively, using full diagonalization techniques. As a result, the convergence region of the NLCE is typically extended to lower temperatures in comparison to high-temperature expansions with the same number of terms.

In Fig. 4, we show results from the NLCE for the t-J model with $J = 0$ for up to the 11th order in the site expansion, where contributions of all clusters with up to 11 sites are considered, for $\mu = 0$ and ± 2.0. By comparing the direct sums in NLCE (thin dashed red lines represent the last two orders) with those from our series, we find that while we have perfect agreement between NLCE and the converged bare sums in the series, the Padé approximants overestimate the value of n in all cases at temperatures lower than one. The convergence of the NLCE results at low temperatures can be further improved using numerical resummations. Here, we show those obtained from the Wynn algorithm [20] by thin solid violet and thick dashed blue lines. Remarkably, the convergence is extended to $T \sim 0.2$ for $\mu = -2.0$, and $T \sim 0.3$ for $\mu = 0$ and 2.0. The results for $\mu = 0$ show that the ground-state density is likely less than 0.525.

In Fig. 5, we plot the chemical potential of the system as a function of temperature for various fixed densities by inverting functions such as those seen in Fig. 4. Here, the dotted dashed lines represent the zeroth-order chemical potential $\mu^{(0)}$ for a fixed density. They all approach zero as $T \to 0$ since they correspond to the atomic limit. The results from the series and the NLCE suggest a different behavior starting at relatively high temperatures for the correlated system, except for the density near 0.5, where the linearity of the chemical potential, and the coincidence with the results from the atomic limit, is extended to low temperatures. This is consistent with the $\mu = 0$ curve in Fig. 3 approaching $n \sim 0.5$ at low temperatures. On the other hand, in the low density Fermi liquid regime, the low-temperature chemical potential is expected to be proportional to T^2. We find that the resumed NLCE results for $n = 0.1$ agree with this behavior as they provide a reasonable fit to the function $A + BT^2$, as shown by a light blue (light gray) line in Fig. 5.

Another feature seen in the plots of chemical potential at fixed density, with potentially important implications for the state of the system, is the change in sign of the slope of μ vs T at low temperatures. Recent theories of thermopower of correlated systems identify the Kelvin formula for thermopower

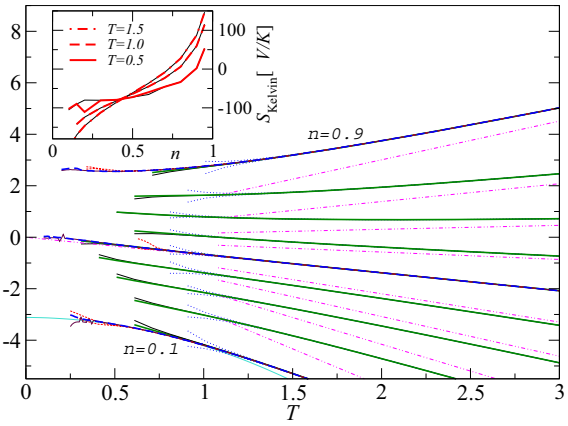

FIG. 5. (Color online) Chemical potential μ at fixed density vs temperature for densities from $n = 0.1$ to $n = 0.9$ (from bottom to top with the increment of $\Delta n = 0.1$). The lines are the same as in Fig. 4, except that the dotted-dashed magenta lines are the zeroth order of the chemical potential in the atomic limit, i.e., $\mu^{(0)} = T \log \frac{n}{2(1-n)}$, and that thin solid lines are Padé$_{\{6,3\}}$. Here, we show the NLCE results for $n = 0.1$, 0.5, and 0.9. The light blue (light gray) solid line is the fit of the low-temperature NLCE results for $n = 0.1$ after resummation to $A + BT^2$ with $A = -3.12$ and $B = -1.10$. The inset shows the Kelvin thermopower, S_{Kelvin}, from NLCE as defined in Eq. (18), in units of microvolts per degree Kelvin vs density. At each temperature, the two lines correspond to different Wynn resummations.

[27,28] by the expression,

$$S_{\text{Kelvin}} = \frac{-1}{q_e}\left(\frac{\partial \mu}{\partial T}\right)_{N,V} = \frac{1}{q_e}\left(\frac{\partial S}{\partial N}\right)_{T,V}, \qquad (18)$$

where $q_e = -|e|$ is the electron charge, S the entropy, and a Maxwell relation is employed in the second identity. This formula captures the considerations of Kelvin's famous paper on reciprocity in 1854 [29], within a contemporary setting. As explained in Refs. [27,28], this expression represents the "thermodynamic" contribution to the true thermopower in addition to the dynamical contributions, that are assumed small in many correlated systems and neglected here. We see from this expression that a flat chemical potential in temperature implies a maximum in entropy at the corresponding density, and locates a density where the thermopower changes sign (from electronlike to holelike), as often seen in correlated systems. From Fig. 5, we observe that $\frac{\partial \mu}{\partial T} > 0$ and hence the Kelvin thermopower is positive for densities close to half filling, whereas near the empty band things are reversed and we get electronlike thermopower. The change in sign seems to arise at a density n between 0.7 and 0.9, somewhat greater than the value $n = \frac{2}{3}$ from the naive atomic limit. A detailed discussion of the thermopower, and the related Hall constant in cuprates and in the two-dimensional t-J model can be found in Refs. [28,30].

In Fig. 6, we show the analog of the quasiparticle fraction defined in the Matsubara frequency space as

$$Z_0(k) = \left[1 - \frac{\text{Im}\,\Sigma(\omega_0, k)}{\omega_0}\right]^{-1}, \qquad (19)$$

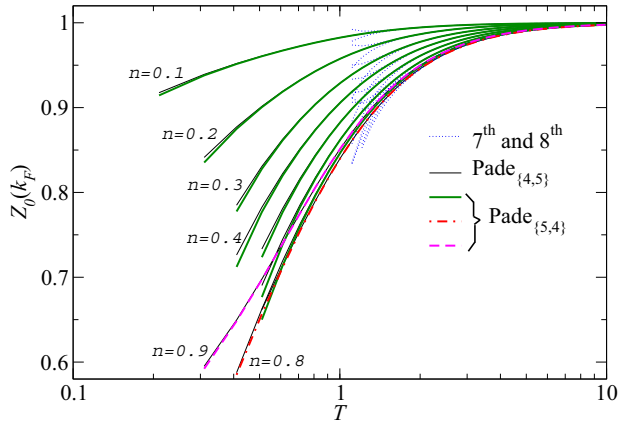

FIG. 6. (Color online) The quasiparticle fraction, defined in the Matsubara frequency space, at the nodal Fermi surface of the corresponding free Fermi gas, Eq. (19), after Padé approximation vs temperature for different values of density. At temperatures below one, the quasiparticle fraction initially decreases with increasing the density before increasing again for $n > 0.7$. The green thick solid lines are for $n = 0.1 \ldots 0.7$ from top to bottom.

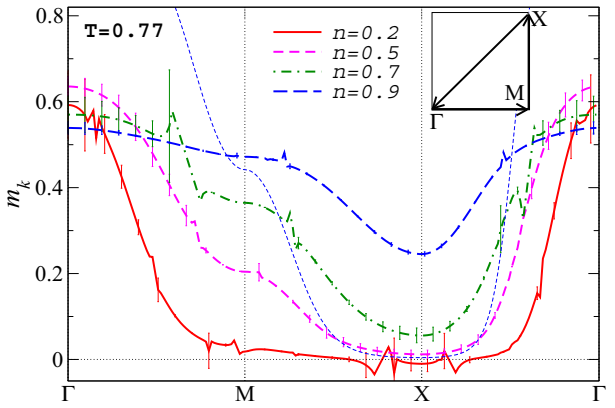

FIG. 7. (Color online) Momentum distribution function at $T = 0.77$ for $n = 0.2, 0.5, 0.7$, and 0.9 vs momentum, as obtained from the average of the two Padé approximations ({4,5} and {5,4}), around the irreducible wedge of the Brillouin zone as shown in the inset. Vertical lines show the difference between the two Padé approximants. The thin dashed line is the momentum occupation number of a free Fermi gas for $n = 0.9$ at the same temperature.

where $\omega_0 = \pi T$ is the lowest Matsubara frequency, as a function of temperature at various densities. We choose the momentum k to be the nodal Fermi vector of a free Fermi gas with the same density (k_F). Previous studies based on the ECFL [2], or high-temperature expansions [31], suggest that this model possesses a Fermi surface coinciding with that of the free Fermi gas. The quantity in Eq. (19) will be equal to the actual quasiparticle fraction deduced from the self-energy in the real frequency axis, $Z(k) = [1 - \frac{\partial \Sigma(\omega,k)}{\partial \omega}|_{\omega \to 0}]^{-1}$, in the limit $T \to 0$. Therefore, the lowest temperatures we have access to may not be low enough to provide us with useful insight as to how the ground-state value of this quantity may vary with density. However, already at $T \sim 0.5$, Padé approximants offer an unexpected insight. We find that $Z_0(k)$ decreases monotonically by increasing the density for $n < 0.8$, then increases as n increases to 0.9. Interestingly, the onset of this change of behavior coincides with that of the change of sign in the thermopower discussed earlier. As $n \to 1$, we do expect the true ground-state value of $Z(k)$ to vanish, therefore this nonmonotonic dependence is presumably an artifact resulting from the finite T definition employed.

In Fig. 7, we show the momentum occupation number, $m_k = \langle c^\dagger_{k\sigma} c_{k\sigma} \rangle$, versus k at $T = 0.77$ for different total densities. Features of this quantity at much lower temperatures were discussed in Ref. [5] for the t-J model. However, the value of the density in the latter study was limited to $n \lesssim 0.75$. Here, we find that even at high temperatures, as the density approaches half filling, there is a huge redistribution of occupations in comparison to the free Fermi gas, as evidenced by the difference in m_k for $n = 0.9$ between the two cases as seen in Fig. 7.

In a recent publication [14], the first moments of the electronic spectral functions of this model were studied using the same series expansion. It was shown that a modified first moment, (the "greater" moment) can better capture the location of the spectral peak at higher densities than the symmetric first moment. More information about the spectral properties of electrons in this model can be gathered from higher order moments, also accessible through the series. In Fig. 8, we show the width of the quasiparticle peak, or the inverse lifetime, defined as

$$\Gamma^{-1}(k) = \sqrt{\varepsilon_2^>(k) - [\varepsilon_1^>(k)]^2}, \tag{20}$$

where $\varepsilon_1^>(k)$ and $\varepsilon_2^>(k)$ are the first and second greater moments, respectively, obtained from the series as described in Eq. (7) of Ref. [14]. Since the spectral function is largely skewed at higher densities [4], the width generally grows as the density increases.

VI. SPECTRAL FUNCTIONS

We next turn to a study of the spectral functions $\rho_G(k,\omega)$, denoted by $A(\omega,k)$ in standard photoemission studies. This can be found from the usual relation $\rho_G(\omega,k) \equiv -\frac{1}{\pi} \mathrm{Im}\, G(\omega + \mu^{(0)} + i\eta, k)$, and requires a knowledge of the Greens function

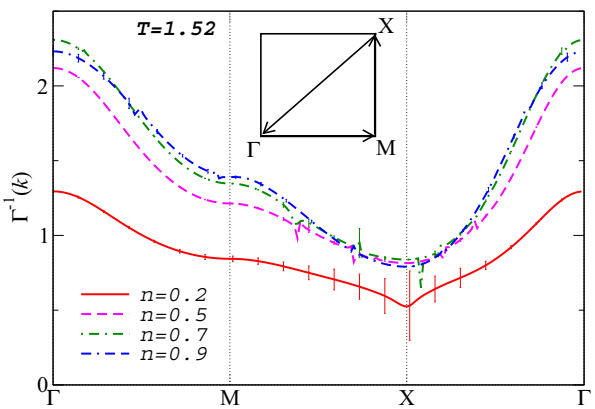

FIG. 8. (Color online) Inverse lifetime, defined in Eq. (20), at $T = 1.52$ and for $n = 0.2, 0.5, 0.7$, and 0.9 vs momentum around the irreducible wedge of the Brillouin zone shown in the inset. $t = 1$ sets the unit of energy. Lines are the same as in Fig. 7.

for complex frequencies. To extract spectral functions, we represent our Green's function as a continued fraction, which, when Taylor expanded to eighth order, reproduces Eq. (16). That is, we write G as (see Ref. [15] for the notation)

$$G(z,k) = \frac{a_G}{z+b_1-}\,\frac{a_1}{z+b_2-}\,\frac{a_2}{z+b_3-}\,\frac{a_3}{z+b_4-}\,\frac{a_4}{z}, \quad (21)$$

where $a_l > 0$ and b_l are real. As explained in Ref. [15] (see also [16]), these conditions ensure that the resulting spectral function obtained from analytic continuation is positive definite. The formulas for the a_l and b_l can be obtained by suitably combining the "raw" moments; this procedure is detailed in Ref. [32]. In the infinite-U Hubbard model, we know *a priori* how many floors will be in the continued fraction representation of a Green's function series of a given order. This is because the constants b_l have units of energy (and must therefore to leading order go like t), and the constants a_l have units of energy squared (and must therefore to leading order go like t^2). Therefore, we know that Eq. (21) is the correct, i.e., maximal continued fraction form obtainable from our eighth-order series. This is an advantage over the case of the finite-U Hubbard model (see Ref. [16]), where the presence of the energy scale U means that the number of floors necessary to represent a series of a given order must be determined empirically.

In Ref. [3], Shastry establishes the relationship between the continued fraction representation of the Green's function [Eq. (21)], and a representation in terms of an infinite sequence of self-energies with spectral densities $\rho_\Sigma^{(n)}(\omega)$, with $n = 0,1,\ldots$. For the standard self-energy we omit the superscript so that $\rho_\Sigma^{(0)}(\omega) \equiv \rho_\Sigma(\omega)$. This is a particularly convenient reformulation of the well-known Mori scheme [33] for relaxation processes, where Laplace transforms over time-dependent correlations are used. In particular, denoting $\Sigma_\infty \equiv \lim_{z\to\infty}\Sigma(z)$, and recalling that

$$G(z,k) = \frac{a_G}{i\omega + \mu - a_G\,\epsilon_k - \Sigma_\infty - \int d\nu\,\frac{\rho_\Sigma(\nu)}{i\omega-\nu}},$$

$b_1 = -a_G\,\epsilon_k - \Sigma_\infty$, and the standard self-energy is expressed as

$$\int \frac{\rho_\Sigma(\nu-\mu^{(0)})}{z-\nu}\,d\nu = \frac{a_1}{z+b_2-}\,\frac{a_2}{z+b_3-}\,\frac{a_3}{z+b_4-}\,\frac{a_4}{z}, \quad (22)$$

where $\rho_\Sigma(\omega) \equiv -\frac{1}{\pi}\mathrm{Im}\,\Sigma(i\omega_n \to \omega + i\eta)$. Following [3], we identify the constant $a_1 \equiv a_\Sigma \equiv \int \rho_\Sigma(\nu)d\nu$, $b_2 \equiv -\Sigma_\infty^{(1)}$, and

$$\int \frac{\rho_\Sigma^{(1)}(\nu-\mu^{(0)})}{z-\nu}\,d\nu = \frac{a_2}{z+b_3-}\,\frac{a_3}{z+b_4-}\,\frac{a_4}{z}. \quad (23)$$

For $l > 1$, one has the general formula,

$$a_l = a_{\Sigma^{(l-1)}}; \quad b_l = -\Sigma_\infty^{(l-1)}. \quad (24)$$

The Green's function of Eq. (21) will lead to a spectral function with a small number of well-separated poles and residues. To obtain a continuous shape for the spectral function, there are several alternatives. We initially follow the procedure of Tomita and Mashiyama (TM) [34], which is useful in the spin relaxation problems, but does not seem to have features of a fermionic self-energy function built into it. Nevertheless, we try it out in view of its simplicity, and as it provides a counterpoint to our preferred method presented next. In the spirit of Ref. [34], we assume that

$$\rho_\Sigma(\omega-\mu^{(0)}) = A\exp[-\alpha^2(\omega-\omega_0)^2], \quad (25)$$

so that the coefficients A,α,ω_0 are fixed using the moments, and higher moments are forced to be those of the Gaussian. Using Eq. (22), we can solve for A, α, and ω_0 in terms of a_1, a_2, and b_2. It is also possible to obtain a continuous spectral function whose moments correctly reproduce all of the coefficients in Eq. (21) by making the Gaussian approximation for the second-level self-energy:

$$\rho_\Sigma^{(2)}(\omega-\mu^{(0)}) = A\exp[-\alpha^2(\omega-\omega_0)^2]. \quad (26)$$

Then, using the relation,

$$\int \frac{\rho_\Sigma^{(2)}(\nu-\mu^{(0)})}{z-\nu}\,d\nu = \frac{a_3}{z+b_4-}\,\frac{a_4}{z+\cdots}, \quad (27)$$

we can solve for A, α, and ω_0 in terms of a_3, a_4, and b_4. However, as shown in Fig. 9 below, this is actually a worse approximation as it accentuates an unphysical sharp peak in the TM scheme spectral function.

An alternative scheme for obtaining continuous spectral functions makes use of our knowledge of the approximate form of the self-energy as $(T,\omega) \to 0$ [7]:

$$\rho_\Sigma(\omega) = A(\omega^2+\pi^2T^2)\left(1-\frac{\omega}{\Delta}\right)\exp\left[-\frac{\omega^2+\pi^2T^2}{\omega_c^2}\right]. \quad (28)$$

Here, $(\omega^2+\pi^2T^2)$ is the standard Fermi-liquid form, $\frac{1}{\Delta}$ provides the aforementioned particle-hole asymmetry, and the exponential extrapolates the low-energy answer to higher energies in a natural way [2]. Once again, we can solve for A, Δ, and ω_c in terms of a_1, a_2, and b_2 by using Eq. (22).

We obtain the spectral function $\rho_G(\omega,k)$ using both Eqs. (25) and (28) at $T = 1.1$ for $n = 0.7$ and $n = 0.9$ and at various points along the irreducible wedge of the Brillouin

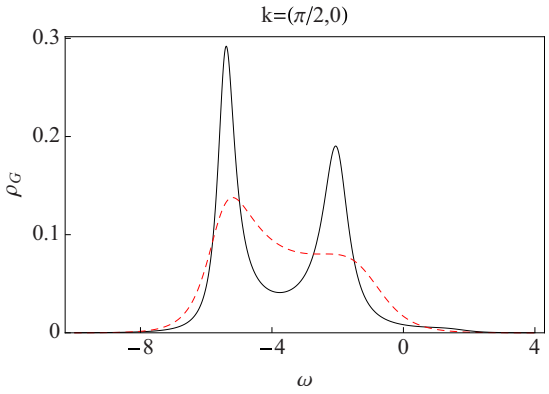

FIG. 9. (Color online) The spectral density for the physical Green's function vs ω for $T = 1.1$ and $n = 0.9$. $t = 1$ sets the unit of energy. The red (dashed) curve is obtained from the TM scheme with the self-energy Eq. (25) and the black (solid) curve is obtained from the TM scheme with the second level self-energy [Eq. (26)]. The latter accentuates the unphysical secondary peak of the TM scheme spectral function.

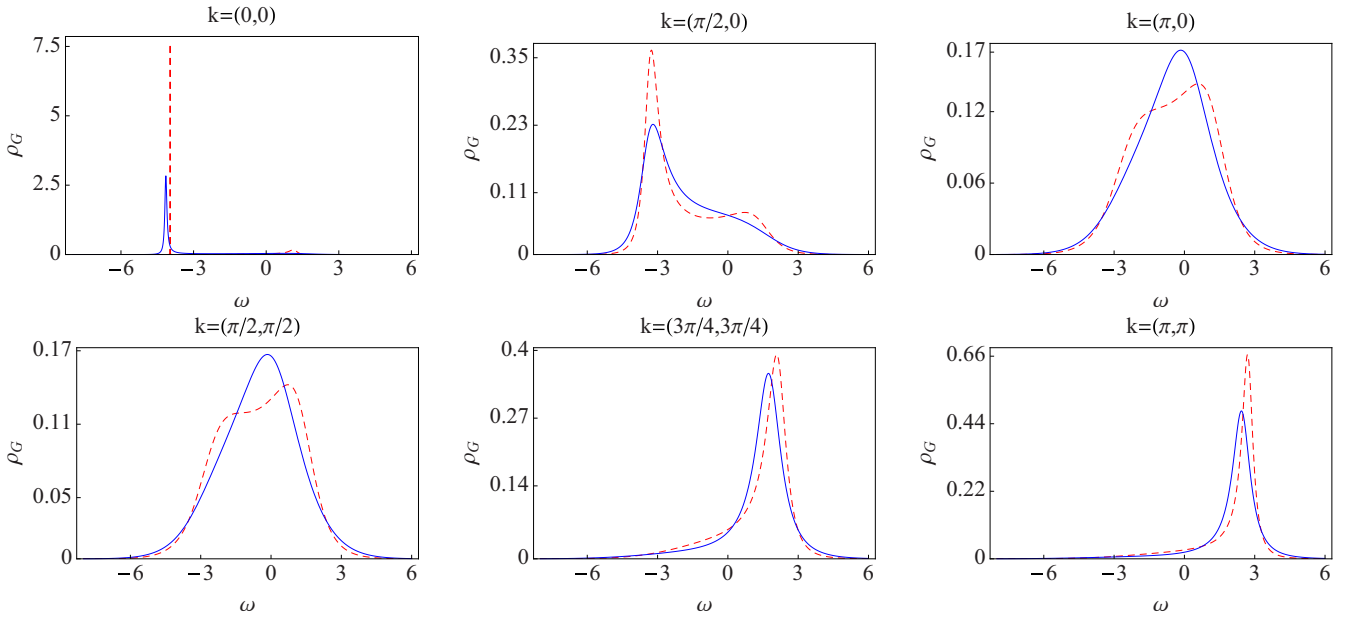

FIG. 10. (Color online) The spectral density for the physical Green's function vs ω for $T = 1.1$ and $n = 0.7$. The blue (solid) curve is obtained from the Fermi-liquid-type scheme [Eq. (28)] and the red (dashed) curve is obtained from the TM scheme [Eq. (25)]. The fairly sharp extra peaks obtained from the TM scheme, as compared to the Fermi-liquid scheme, seem to be physically unreasonable. We also note that the spectral functions from ECFL found numerically using the $O(\lambda^2)$ scheme (see Fig. 3(f) of Ref. [14]) find rather broad peaks at high T.

zone. The spectral functions $\rho_G(\omega,k)$ are plotted in Fig. 10 for $n = 0.7$ and in Fig. 11 for $n = 0.9$.

VII. SUMMARY

We present an implementation of the linked-cluster expansion for the Green's function of the infinite-U Hubbard model on a computer, which is based on a formalism proposed by Metzner [1]. Using efficient algorithms on parallel computers, we have carried out the expansion up to the eighth order in terms of the hopping amplitude, and obtained analytic results for the Green's function and the Dyson-Mori self-energy on the square lattice as a function of momentum and Matsubara frequency at a given fixed density. Since the lattice sums for graphs in this approach are evaluated independently of their time integrals and spin sums, our implementation paves the

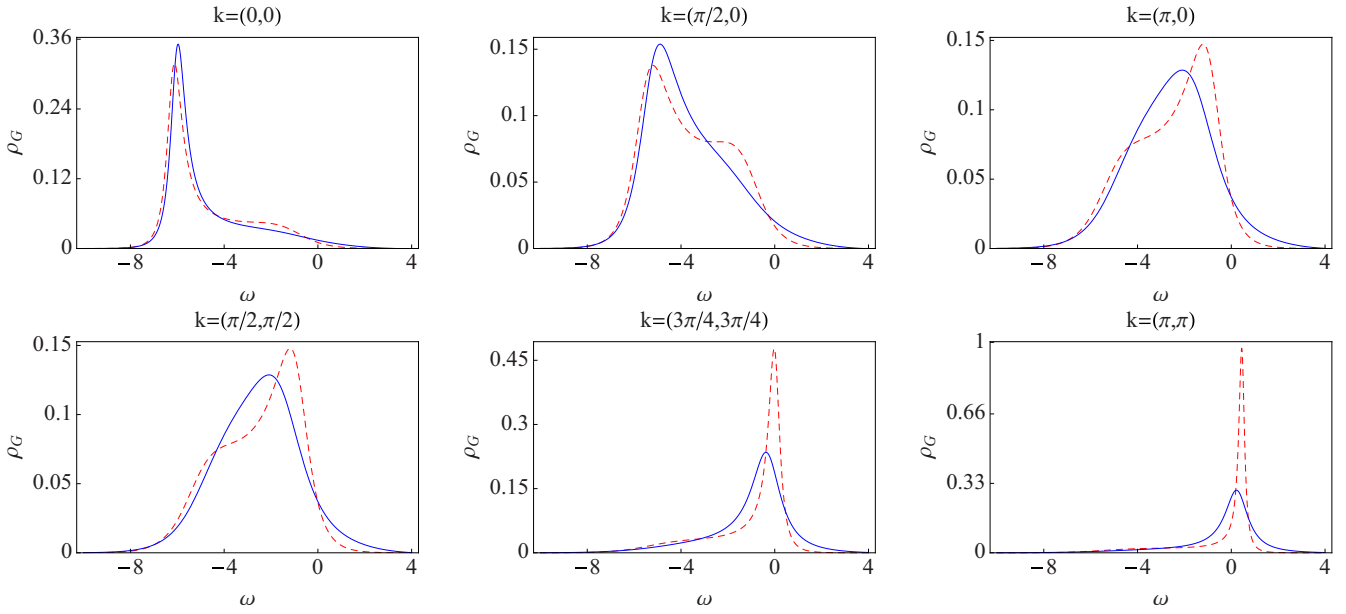

FIG. 11. (Color online) The spectral density for the physical Green's function vs ω for $T = 1.1$ and $n = 0.9$. Lines are the same as in Fig. 10.

way for obtaining similar results for other geometries and spatial dimensions.

To extend the region of convergence in temperature, we employ Padé approximations and study several static and dynamic quantities. The equation of state exhibits significant deviations from the atomic limit starting at relatively high temperatures and reveals interesting trends near $n = 0.5$, where we find that the chemical potential changes linearly with temperature and remains very close to the one in the atomic limit down to the lowest temperatures accessible to us. We also find that the change in sign of the derivative of μ with respect to T at constant density, which is proportional to the thermopower in Kelvin's formula, takes place at increasingly higher densities due to correlations as the temperature is lowered. The momentum distribution function also shows significant deviations from free fermions, and becomes more uniform across the Brillouin zone as the correlations build up at higher densities. We further study dynamic quantities, such as the analog of the quasiparticle fraction in the Matsubara frequency space vs temperature, which shows a nonmonotonic dependence on density at low temperatures, and the lifetime of the quasiparticles at various densities, obtained in the series through the first two moments of the electronic spectral functions. To make contact with experiments and extend previous results for the spectral functions obtained within the ECFL or the dynamical mean-field theory, we calculate them here after transforming the Green's function series to continued fractions, or by employing certain forms for the spectral functions suggested by the ECFL theory. We present our results for densities close to half filling at several points in the momentum space.

To benchmark our results from the Padé approximations for the equation of state at temperatures lower than the hopping amplitude, where the direct sums in the series do not converge, and to shed more light on the state of the system at those temperatures, we also present results from the NLCE up to eleventh order for an equivalent model, i.e., the t-J model with $J = 0$. We find perfect agreement between the direct sums from the two methods when they converge, and that at lower temperatures, the Padé approximants generally overestimate the density for a given chemical potential. The NLCE results after numerical resummations also help obtain the thermopower vs density at a temperature that is not otherwise accessible to the series even after the Padé approximations.

ACKNOWLEDGMENT

This work was supported by DOE under Grant No. FG02-06ER46319 (B.S.S. and E.P.), and by NSF under Grant No. OCI-0904597 (E.K. and M.R.).

APPENDIX A: RECURSIVE EXPANSION OF CUMULANTS

In the following, we combine the time and spin variables and denote them by their index only, i.e., $C^0_m(\tau_1\sigma_1, \ldots \tau_m\sigma_m|\tau'_1\sigma'_1, \ldots \tau'_m\sigma'_m) \to C^0_m(1, \ldots m|1', \ldots m')$. Cumulants are calculated by taking functional derivatives of a generating functional with respect to Grassmann variables [1,21], and can be expressed in terms of UGFs. We give explicit expressions for C^0_m through $m = 3$.

$$C^0_1(1|1') = G^0_1(1|1'), \quad C^0_2(1,2|1',2') = G^0_2(1,2|1',2') - G^0_1(1|1')G^0_1(2|2') + G^0_1(1|2')G^0_1(2|1'), \tag{A1}$$

$$\begin{aligned} C^0_3(1,2,3|1',2',3') = {} & G^0_3(1,2,3|1',2',3') - C^0_2(1,2|1',2')G^0_1(3|3') + C^0_2(1,2|1',3')G^0_1(3|2') - C^0_2(1,2|2',3')G^0_1(3|1') \\ & + C^0_2(1,3|1',2')G^0_1(2|3') + C^0_2(1,3|2',3')G^0_1(2|1') - C^0_2(1,3|1',3')G^0_1(2|2') \\ & - C^0_2(2,3|1',2')G^0_1(1|3') - C^0_2(2,3|2',3')G^0_1(1|1') + C^0_2(2,3|1',3')G^0_1(1|2') \\ & - G^0_1(1|1')G^0_1(2|2')G^0_1(3|3') + G^0_1(1|1')G^0_1(2|3')G^0_1(3|2') + G^0_1(1|2')G^0_1(2|1')G^0_1(3|3') \\ & - G^0_1(1|2')G^0_1(2|3')G^0_1(3|1') + G^0_1(1|3')G^0_1(2|2')G^0_1(3|1') - G^0_1(1|3')G^0_1(2|1')G^0_1(3|2'). \end{aligned} \tag{A2}$$

The rule for obtaining the expansion for $C^0_m(1, \ldots m|1', \ldots m') - G^0_m(1, \ldots m|1', \ldots m')$ is as follows. Partition the unprimed integers $1 \ldots m$ into at least two sets. Each set in the partition corresponds to a cumulant, in which the unprimed numbers in the set are written in ascending order. The primed numbers $1' \ldots m'$ are then partitioned amongst the cumulants created by the unprimed number partitions, and are also written in ascending order. The sign of the term is $(+)$ if the permutation to get from primed to unprimed numbers is odd, and $(-)$ if it is even. The sign is due to the Grassmann variables in the generating functional, and is ultimately a consequence of the fermionic nature of the operators. $C^0_3(1,2,3|1',2',3')$ can be expressed in terms of the UGFs by plugging Eq. (A1) into Eq. (A2). In general, $C^0_m(1, \ldots m|1', \ldots m')$ can be obtained in terms of UGFs of equal or lower orders by this recursive procedure.

APPENDIX B: TIME INTEGRALS

In evaluating the time integrals, we use the following general result for the time integral of a product of step functions in terms of a series of ordered internal times τ_i, over which the integrals are taken, and a fixed external time τ:

$$\begin{aligned} & \int_0^\beta d\tau_n \int_0^\beta d\tau_{n-1} \ldots \int_0^\beta d\tau_2 \int_0^\beta d\tau_1 \Theta(\tau_n - \tau_{n-1})\Theta(\tau_{n-1} - \tau_{n-2}) \ldots \Theta(\tau_{m+1} - \tau)\Theta(\tau - \tau_m) \ldots \Theta(\tau_3 - \tau_2)\Theta(\tau_2 - \tau_1) \\ & = \frac{\tau^m(\beta - \tau)^{n-m}}{m!(n-m)!}. \end{aligned} \tag{B1}$$

[1] W. Metzner, Phys. Rev. B **43**, 8549 (1991).

[2] B. S. Shastry, Phys. Rev. Lett. **107**, 056403 (2011); **108**, 029702 (2012); Phys. Rev. B **87**, 125124 (2013).

[3] B. S. Shastry, Phys. Rev. B **84**, 165112 (2011).

[4] B. S. Shastry, Phys. Rev. Lett. **109**, 067004 (2012).

[5] D. Hansen and B. S. Shastry, Phys. Rev. B **87**, 245101 (2013).

[6] B. S. Shastry, E. Perepelitsky, and A. C. Hewson, arXiv:1307.3492; Phys. Rev. B **88**, 205108 (2013).

[7] R. Zitko, D. Hansen, E. Perepelitsky, J. Mravlje, A. Georges, and B. S. Shastry, Phys. Rev. B **88**, 235132 (2013).

[8] E. Perepelitsky and B. S. Shastry, Ann. Phys. **338**, 283 (2013).

[9] A. Georges, G. Kotliar, W. Krauth, and M. J. Rozenberg, Rev. Mod. Phys. **68**, 13 (1996).

[10] X. Deng, J. Mravlje, R. Zitko, M. Ferrero, G. Kotliar, and A. Georges, Phys. Rev. Lett. **110**, 086401 (2013).

[11] G. Palsson and G. Kotliar, Phys. Rev. Lett. **80**, 4775 (1998).

[12] L. F. Arsenault, B. S. Shastry, P. Sémon, and A.-M. S. Tremblay, Phys. Rev. B **87**, 035126 (2013).

[13] G. H. Gweon, B. S. Shastry, and G. D. Gu, Phys. Rev. Lett. **107**, 056404 (2011); K. Matsuyama and G. H. Gweon, *ibid.* **111**, 246401 (2013).

[14] E. Khatami, D. Hansen, E. Perepelitsky, M. Rigol, and B. S. Shastry, Phys. Rev. B **87**, 161120 (2013).

[15] J. A. Shohat and J. D. Tamarkin *The Problem of Moments* (American Mathematical Society, Providence, 1943).

[16] S. Pairault, D. Senechal, and A.-M. S. Tremblay, Eur. Phys. J. B **16**, 85 (2000).

[17] M. Plischke, J. Stat. Phys. **11**, 159 (1974); K. Kubo and M. Tada, Progr. Theor. Phys. **69**, 1345 (1983); **71**, 479 (1984); K. K. Pan and Y. L. Wang, Phys. Rev. B **43**, 3706 (1991); M. Bartkowiak and K. A. Chao, *ibid.* **46**, 9228 (1992); W. O. Putikka, M. U. Luchini, and R. R. P. Singh, Phys. Rev. Lett. **81**, 2966 (1998); V. W. Scarola, L. Pollet, J. Oitmaa, and M. Troyer, *ibid.* **102**, 135302 (2009); L. De Leo, J.-S. Bernier, C. Kollath, A. Georges, and V. W. Scarola, Phys. Rev. A **83**, 023606 (2011).

[18] There have been a number of efforts to perform a strong-coupling expansion for the Green's function in a self-consistent manner, i.e., by resuming an infinite subclass of diagrams [16,19].

[19] L. Craco and M. A. Gusmao, Phys. Rev. B **52**, 17135 (1995); **54**, 1629 (1996); L. Craco, J. Phys.: Condens. Matter **13**, 263 (2001); M. E. Foglio, T. Lobo, and M. S. Figueira, arXiv:0903.0139; T. Lobo, M. S. Figueira, and M. E. Foglio, Nanotechnology **21**, 274007 (2010).

[20] M. Rigol, T. Bryant, and R. R. P. Singh, Phys. Rev. Lett. **97**, 187202 (2006); Phys. Rev. E **75**, 061119 (2007).

[21] J. W. Negele and H. Orland, *Quantum Many-Particle Systems* (Addison-Wesley, New York, 1988).

[22] A. A. Abrikosov, L. Gorkov, and I. Dzyaloshinski, *Methods of Quantum Field Theory in Statistical Physics* (Prentice-Hall, Englewood Cliffs, 1963).

[23] This series has also been calculated by hand through fourth order in Ref. [24] using a completely independent method. The results of the two series match exactly.

[24] E. Perepelitsky, arXiv:1310.3797.

[25] Note that when $U = \infty$, the creation and annihilation operators in Eq. (3) become Gutzwiller projected, and hence, follow different anticommutation relations than those valid for canonical fermion operators.

[26] Higher orders for the square lattice or other geometries are available upon request.

[27] M. R. Peterson and B. S. Shastry, Phys. Rev. B **82**, 195105 (2010).

[28] B. S. Shastry, Rep. Prog. Phys. **72**, 016501 (2009).

[29] W. Thomson (Lord Kelvin), Proc. R. Soc. Edinburgh 123, Collected Papers I, 23741 (1854).

[30] A. Garg, B. S. Shastry, K. B. Dave, and P. Phillips, New J. Phys. **13**, 083032 (2011).

[31] R. R. P. Singh and R. L. Glenister, Phys. Rev. B **46**, 14313 (1992).

[32] M. Dupuis, Prog. Theor. Phys. **37**, 502 (1967).

[33] H. Mori, Prog. Theor. Phys. **33**, 423 (1965).

[34] K. Tomita and H. Mashiyama, Prog. Theor. Phys. **51**, 1312 (1974).